


Article

Study of the Direct Metal Deposition of AA2024 by ElectroSpark for Coating and Reparation Scopes

Paola Leo ¹, Gilda Renna ¹ and Giuseppe Casalino ^{2,*} 

¹ Innovation Engineering Department, University of Salento, Via per Arnesano s.n., 73100 Lecce, Italy; paola.leo@unisalento.it (P.L.); gilda.renna@unisalento.it (G.R.)

² DMMM, Politecnico di Bari, Viale Japigia, 182, 70124 Bari, Italy

* Correspondence: giuseppe.casalino@poliba.it; Tel.: +39-080-596-2753

Received: 20 July 2017; Accepted: 18 August 2017; Published: 14 September 2017

Abstract: ElectroSpark Deposition (ESD) is a pulsed micro-welding process that is capable of depositing wear and corrosion resistance deposit to repair, improve, and to extend the service life of the components and tools. Major new applications have taken place in gas turbine blades and steam turbine blade protection and repair, and in military, medical, metal-working, and recreational equipment applications. In this study, the ESD technique was exploited to fabricate 2024 aluminum alloy deposit on a similar substrate. The deposits were deposited using different process parameters. Heat input was varied on three levels. The outcoming microstructure was analyzed by optical and scanning electron microscopies. The deposit was characterized by the overlapping of layers with a mixed microstructure. The average hardness was independent from the process parameters. Both porosity inside the deposits and cracks at the deposit/substrate interface were detected. The porosity lowered with the heat input and increased the average length of cracks.

Keywords: electrospark; deposition; aluminum alloy; microstructure; defectiveness

1. Introduction

In recent years the deposition processes [1,2] and the repair method [3,4] of some high value components have become more prominent in the aeronautics industry. Cost of equipment, long processing time, and pollution are just some of the disadvantages of the traditional surface treatment processes (such as physical vapor deposition (PVD), chemical vapor deposition (CVD), electroplating, thermal diffusion (TD)) that are widely used to improve anti-wear, anti-corrosion and anti-softening of component material [5]. Besides, the alternative repair imposed by cost criteria is increasingly spreading, instead of the damaged components replacement. Sometimes, the physical and microstructural characteristics of the alloy limit the fusion welding repair techniques [6]. For instance, the fusion welding repair process of AA2024 is not suitable because the alloy is specifically susceptible to hot cracking, both in the welding (solidification cracking) and in the base metal (liquation cracking) [7–13].

ElectroSpark Deposition (ESD) technique consists of a capacitor-based power supply, a consumable electrode, and an applicator (electrode holder). An electrical arc (due to discharge of capacitor) is pulsed between a rotating consumable electrode (anode) and the work piece/substrate (cathode) to produce the deposit by detaching small droplets of material from the electrode and ejecting towards substrate. Pulse frequencies of a few kilohertz, combined with pulses duration in the 1–10 μ s range allow substrate heat dissipation over ~99% of the duty cycle [1,14]. The low net heat input into the substrate, and the ability to bond the deposition to the substrate without metallurgical changes in the heat sensitive substrate are among the advantages of the ESD process [15,16]. Moreover, the high cooling-rates during ESD, on the order of 10^5 – 10^6 °C/s, can produce nano-structured deposits [17], characterized by increased hardness and tribological benefits [16,18].

The deposition parameters regimes (voltage, capacitance, frequency) depend on the type of electrode and its melting temperature, thermal conductivity, chemical reactivity of the anode elements, diffusivity, density, electrical resistance, thermal inertia, and flowability [19].

A wide variety of metals and ceramic/metal deposits are produced by ESD [1,20]. Among them, there are Fe-based alloys [21], superalloys [22–24], and magnesium alloys [25]. Heard and Brochu [26] determined that ESD is a feasible method of producing an aluminum-nickel deposit, consisting of a nano-structured Al_3Ni phase. Cadney and Brochu [27] investigated the feasibility of using the ESD process to deposit amorphous electrode material ($\text{Zr}_{41.2}\text{Ti}_{13.8}\text{Ni}_{10}\text{Cu}_{12.5}\text{Be}_{22.5}$) onto an amorphous substrate of the same composition without crystallizing the deposit or the substrate. Hasanabadi et al. [2] investigated the deposition of $\text{Fe}_{48}\text{Cr}_{18}\text{Mo}_7\text{B}_{16}\text{C}_4\text{Nb}_7$ crystalline alloy on 316L stainless steel substrate. Xie and Wang investigated the ESD of several Ni-based super-alloy systems [28,29], assessing the feasibility of repairing nickel based super-alloy substrates with MCrAlY deposition. Unfortunately, to date, the state of art is very poor of studies regarding the use of ESD technique to deposit thermally sensitive materials such as the 2024 alloy.

In this paper, thick deposits of 2024 aluminum alloy on similar substrate using different process parameters were produced and analyzed. The surface, the macro and microstructure, micro-hardness, and defectiveness of the samples were characterized and discussed for different process parameters. Moreover, since the investigated alloy specifically susceptible to hot cracking, even the relationship between the processing parameters and the cracks in the substrate was investigated. Finally, the suitable process parameters for reducing both porosity in the deposits and the cracks in the substrate were identified.

2. Experimental Setup

The substrate and electrode material is an AA2024-T4 alloy, based on Al-Cu-Mg system. The suffix (T4) indicates that the alloy has been naturally aged (at Room Temperature) after solutionizing. The substrate was supplied as rolled plates 4 mm thick: 80×20 mm strips were cut from the plates. The deposit was deposited up on the strip, performing multiple depositions on the same line along the rolling direction (RD). The scheme of the depositions is shown in Figure 1.

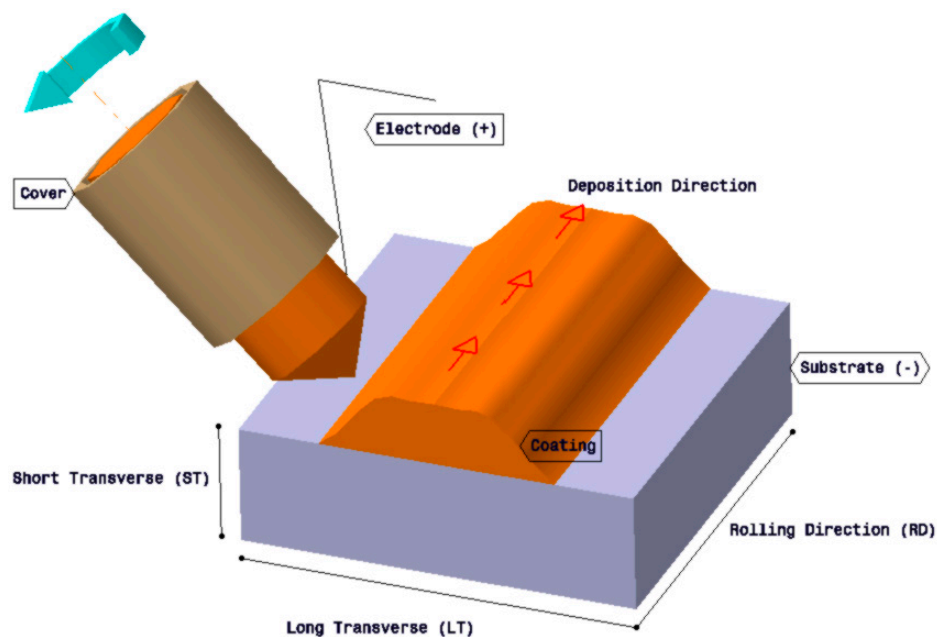


Figure 1. Scheme of ElectroSpark Deposition (ESD) process.

The chemical composition (wt %) of 2024 alloy is listed in Table 1.

Table 1. Chemical composition of AA2024 alloy.

Composition	Ti	Zn	Fe	Cr	Si	Cu	Mn	Mg	Other	Al
AA2024	<0.15	<0.25	<0.5	<0.5	<0.5	3.8–4.9	0.3–0.9	1.2–1.8	<0.15	Bal.

ElectroSpark Deposition was performed using a “Technocoat MicroDepo Model 150” ESD machine (TechnoCoat International, Shizuokaken, Japan). The deposition was carried out at room temperature using a hand-held gun with Ar protection. The Argon was flowed throughout the deposition process at a rate of 10 L/min. Before performing the deposit process, the substrate was polished with 800-grit SiC paper. The rotational speed of the 3 mm diameter electrode was kept constant at 1200 rpm throughout the trials, whereas the other three parameters voltage, capacitance, and frequency, were properly varied. To determine the feasibility of producing thick deposits using the ESD process, for each set of parameters, multiple-layer depositions were performed using 50 subsequent deposition passes. The spark pulse-energy (E_s) in joule (J) of each set parameter given in the Table 2 was determined as follows:

$$E_s = \frac{1}{2} CV^2$$

where C is the capacitance in Farad (F) and V is the voltage in Volt (V); while F is the discharge frequency in Hertz (Hz) [26]. In Table 2 are shown the values of the spark pulse Energies used for processing the samples whereas increasing values of the V , C , and F subscript indicate increasing values of the respective parameters. After the deposition, the deposits were sectioned using a diamond blade on the Short Transverse-Long Transverse, ST-LT, (see Figure 1). The ST-LT sections of the deposits were cold mounted. Then, they were ground and mechanically polished. After that, the specimens were etched using Keller reagent (1 mL HF, 1.5 mL HCl, 2.5 mL HNO₃, and 95 mL H₂O). The analysis of the microstructure was performed by conventional analytical techniques, such as Optical Microscope (OM) Nikon Epiphot 200 (Nikon Inc., Melville, NY, USA) accompanied by a computer-assisted image analysis (NIS Elements AR) and Scanning Electron Microscope (SEM) Zeiss EVO (Zeiss, Jena, Germany) equipped with energy dispersive spectrometry (EDS) technique using a Bruker electron microprobe. The grain structure of BM was revealed, after standard metallographic procedures, through anodizing by Barker’s electrolyte at room temperature with 20 V for 50 s. Both of the voids areas inside the deposit and the length of the cracks at the substrate/deposit interface on ST-LT plane (Figure 1) were obtained for each deposit using NIS software for imaging analysis. Especially, defects percentage were measured as the sum of the defects areas divided by the area of the deposit. The average length of the interface cracks was estimated. Vickers micro-hardness (0.05 kg/15 s) was measured in the deposit cross-section (ST-LT plane). Micro-hardness indentations were arranged parallel to the deposit/substrate interface. Three lines of indentations 100 μ m far each other and from interface were realized. Both the average hardness, resulting from the measurements along each line, and the average hardness considering all the indentation made, was calculated. Moreover, the micro-hardness was measured also in some areas of the deposits showing interesting microstructural features.

Table 2. ESD process parameters for the depositions.

n°	Voltage [V]	Capacitance [μ m]	Frequency [Hz]	E_s [J]
1	V1	C2	F1	0.5
2	V1	C2	F2	0.5
3	V1	C2	F3	0.5
4	V2	C1	F1	0.9
5	V2	C1	F2	0.9
6	V2	C1	F3	0.9
7	V2	C2	F1	1.125
8	V2	C2	F2	1.125
9	V2	C2	F3	1.125

3. Results and Discussion

3.1. Microstructure of AA2024 Al-Cu-Mg Alloy

The microstructure of the substrate cross-section is shown in Figure 2a,b. The optical micrograph (OM) after chemical etchant (Figure 2a) and SEM/EDS analyses (Figure 2b) reveal that the intermetallic particles are mainly roughly spherical Al_2CuMg (n°1 Figure 2a,b) of approximate size 5–10 μm , and light grey CuAl_2 particles (n°2 Figure 2a,b). Moreover $(\text{Mn,Fe})_3\text{SiAl}_{12}$ (light brown n°3 Figure 2a,b) and $\text{Al}(\text{Cu,Fe,Mn})$ phase (dark brown n°4 Figure 2a,b) have been detected. These last particles are as big as 10 μm and with an irregular shape. Furthermore, according to literature [6,30], the fine dispersoids observed in the Al matrix could be both $\text{Cu}_2\text{Mn}_3\text{Al}_{20}$ and/or Al_2Cu . Figure 2c displays the as-cast microstructure of the electrode. The electrode microstructure is homogeneous and consisting of a matrix of Al studded by the same intermetallic particles observed in the substrate but having a smaller size.

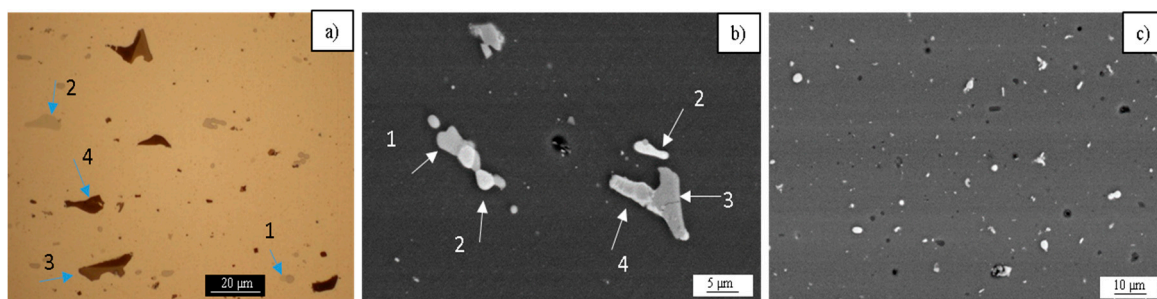


Figure 2. Optical (a) and Scanning Electron Microscope (SEM) micrographs (b,c) of AA2024-T4 substrate (a,b) and electrode (c).

Figure 3 shows the substrate microstructure after anodizing both in the ST-LT (Figure 3a) and in the ST-RD plane (Figure 3b). As expected, the grain structure is elongated, especially in the rolling direction (Figure 3b). Both the planes exhibit the same average micro-hardness ($\text{HV}_{0.05/15}$) equal to 141 ± 2.2 . The average micro-hardness ($\text{HV}_{0.05/15}$) of AA2024 electrode is 124 ± 1 .

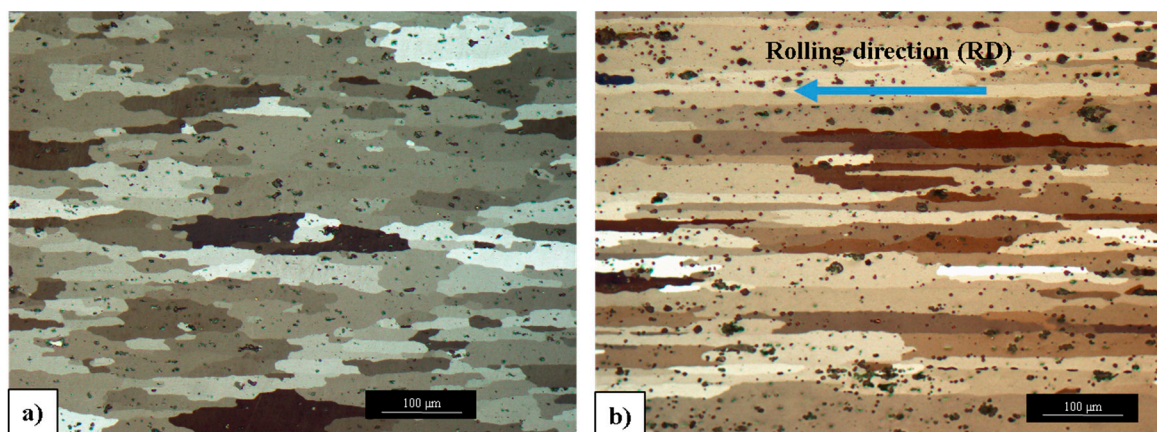


Figure 3. Grain structure in AA2024-T4 polarized light micrographs showing (a) deposit cross-section (ST-LT plane); (b) ST-RD.

3.2. Surface Morphology

Both the typical splash pattern appearance produced by this technique (Figure 4a) and the last splat superimposed on the previous layer is clearly visible. This splash morphology depends on

the arc energy, which melt the electrode tip and result in the formation of the droplet. The molten droplet from the electrode is propelled towards and impinges on the melted or partial melted substrate. The liquid pool rapidly solidifies along with the associated shrinkage. Particularly, the deposit is characterized by peaks and valleys that indicate that the material is deposited in preferential spots. This is mainly due to a plasma pressure effect and irregular gap space between the electrode and substrate. The plasma pressure splashes the liquid pool generating peaks and valleys of solidified material [1,20]. Once generated, those irregularities led to irregular space [1,20] of electrode with substrate. The variation of gap space promotes a higher amount of material mainly on the peaks of the deposit where the electrostatic forces prevail. Of course, even casual local electric field oscillations due to the manual deposition, generate different amount of melted material and irregular deposition. Therefore, the deposit buildup is not uniform and the top surface is uneven.

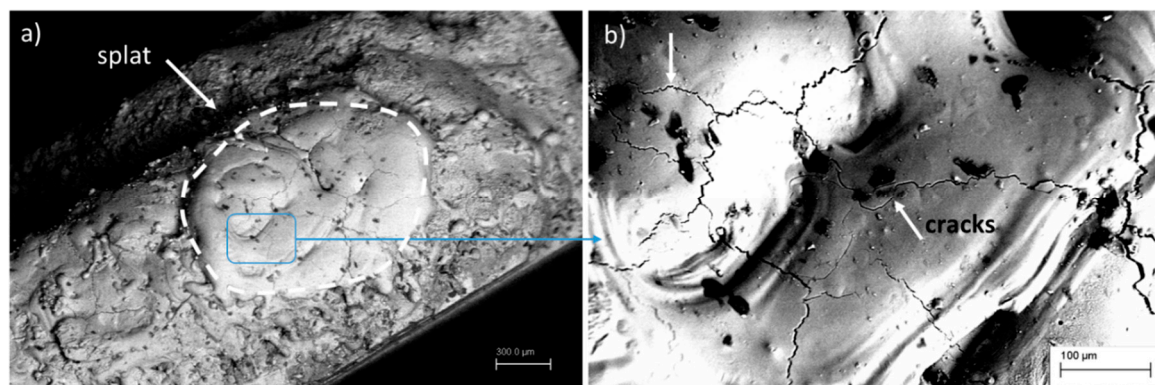


Figure 4. SEM micrograph of the AA2024 deposit surface following a manual ESD deposition: (a) morphology of 50 layer deposits in higher magnification; (b) enlarged image of the spot fringe at 500 \times .

Cracks were observed onto the coated surface (Figure 4b). The formation of these cracks is mainly due to thermal stresses but it can also be generated by the mechanical impact of the electrode tip to the workpiece. Generally, the cracks can nucleate in the first deposited layer and/or on defects (voids) inside the deposit. Thereafter, they are usually propagated upwards by the thermal stress, which produces well-delimited regions on the coated surface (Figure 4b). Those cracks propagate perpendicular to the substrate and they can be clearly observed in the deposits cross-section (Figure 5). Some cracks propagated parallel to the substrate and to the deposit/substrate interface (delamination cracks). That was due to the cooler bulk of the substrate, which prevents the shrinkage during the solidification of the molten metal that is transferred to the substrate from the electrode [31,32].

The deposit cross-section exhibits several discontinuities, i.e., voids. It was observed small spherical voids (gas porosity n°1), large, random shaped voids (bridging porosity n°2), and thin void layers (laminar porosity n°3). The formation of these discontinuities depends greatly on the amount of material that led to fusion during the process and its distribution (Figure 5).

3.3. Microstructure

Deposit microstructure is independent of process parameters. Figure 6 shows the ESD morphology in the deposit longitudinal section (perpendicular to the ESD buildup direction). The surface is characterized by the impact of a single splat having a well-defined interface, which forms between them by fusion and diffusion reactions [32]. Some of those interfaces are highlighted by dashed lines in Figure 6a. The microstructure at interface, see the arrows in Figure 6a, was resolved at higher magnification in Figure 6b,c. It is non-uniform and contains mainly equiaxed dendrites (Figure 6b) with an unclear dendritic morphology (Figure 6c). Dendritic morphology is highlighted by the second phase segregation (light color) at the interspacing. The splats microstructure is also not uniform. In A and B areas in Figure 6b,c, the microstructure is characterized by cellular dendrites of assorted size.

The microstructure of each splat can result not uniform as shown in the areas D and E in Figure 6b. The solidification microstructure depends on the local solidification conditions, i.e., the rate of growth V [mm/s] and the temperature gradient G [$^{\circ}\text{C}/\text{mm}$] at the solid/liquid interface [33]. The ratio of G to V , namely G/V , determines the features of the solidification microstructure [23]. The smaller is the ratio of G/V , the greater is the tendency to equiaxed dendritic growth. While, high values of the ratio of G/V lead to cellular dendritic or cellular growth until to planar growth mode. Owing to manual process of deposition, the deposition rate, the distance of the electrode to work-piece surface and the force on the electrode are difficult to keep constant. As a result, the local heat input and the thickness of the splat vary at different points, which affect the solidification conditions and the resulting microstructure. Moreover, since the product $G \times V$ (equivalent to cooling rate) governs the scale of the solidification structure (the greater the cooling rate and the finer the scale of microstructure), the size of the microstructure would vary at different points. Generally, the microstructure scale is quite fine as each splat is always characterized by small volume of molten metal (even if variable due to manual process) and undergoes very high cooling rates in contact with the cold substrate.

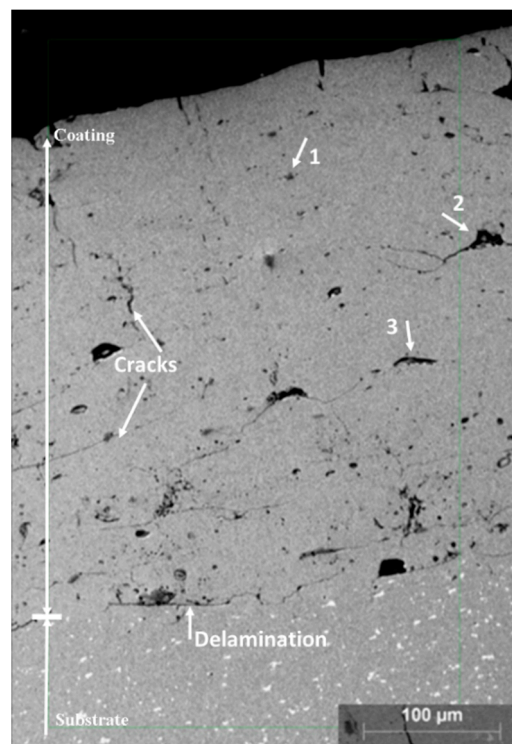


Figure 5. SEM image of multiple-layer deposit (cross-section) produced using 50 deposition passes and shield gas Ar: spherical voids (gas porosity $n^{\circ}1$), large, random shaped voids (bridging porosity $n^{\circ}2$) and thin void layers (laminar porosity $n^{\circ}3$).

The cross-section morphology of AA2024 electrospark deposit (parallel to the build direction) is shown in Figure 7. Figure 7a,b show optical and SEM micrograph, respectively. The deposit consists of several stacked splats [32]. The layered structures can be seen in Figure 7a, where layer-layer and layer-substrate interfaces are shown. The microstructure of the deposit cross-section is characterized by grains that have the same crystallographic orientation. The grains are columnar (parallel to the growth direction of the deposit) and nucleate epitaxially on the grains of the substrate [9,34,35]. For this reason, the columnar grain boundaries of the deposit are along the grain boundaries of the substrate and form a continuous network (Figure 4a). The grain boundaries have been highlighted in Figure 7a,b. Usually, columnar grains contain more than one layer and grow through the whole deposit from the surface of the substrate (Figure 7a) [36].

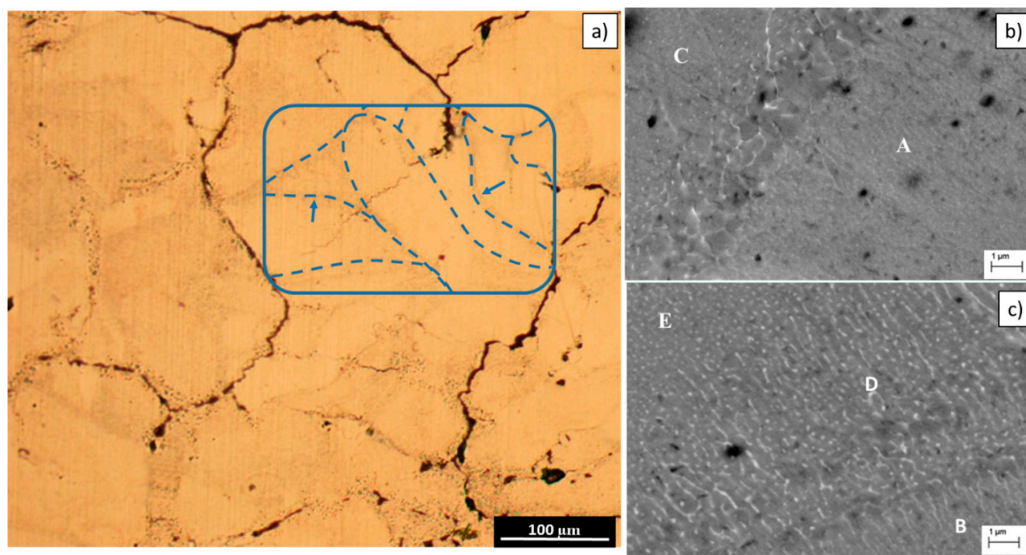


Figure 6. Overview of longitudinal-section of the deposit: (a) longitudinal-section morphology of ESD layer from top view showing sequence of deposition of ESD splats in the same plane of view (the arrow indicates the interface formed between the splat); (b,c) SEM images showing different zone with fine microstructure and splat-splat interface.

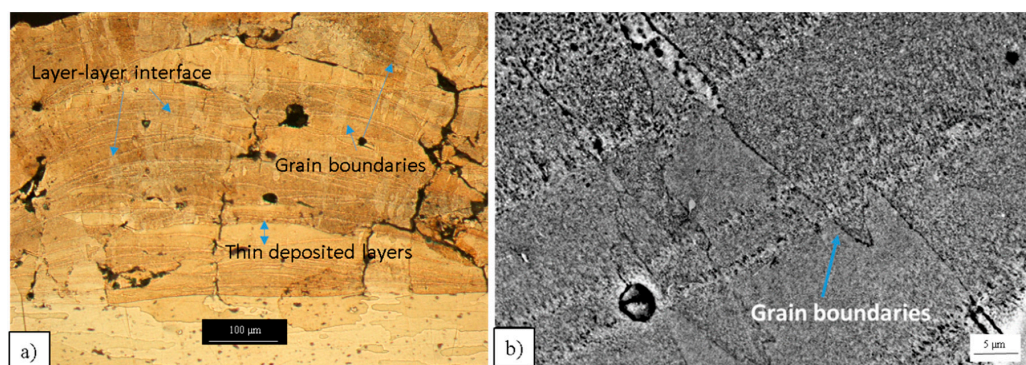


Figure 7. Overview of deposit cross-section: (a) Optical Microscope (OM) Nikon Epiphot image showing the microstructural of built-up layered deposit and (b) SEM micrograph showing the boundary of slender columnar like grain vertical to the build direction.

Figure 8 shows SEM micrographs for some different areas inside of the deposit cross-section. The microstructural scale and morphology are non-uniform but strongly variable (Figure 8), as it was discussed in the above paragraph (Figure 6). Particularly, the layer-layer interfaces microstructure exhibits either equiaxed dendrites (highlighted in Figure 8a) or undefined dendrites morphology (highlighted in Figure 8b). Moreover, the different layers can exhibit the same cellular dendritic microstructure (highlighted by the circles A and B in Figure 8c) or different microstructures (highlighted by the circles C and D in Figure 8a). Moreover, inside of the same layer, both a dendritic morphology (circle E in Figure 8b) and a uniform distribution of fine second phase particles (circle F, Figure 8b) can be observed. The cellular dendrites, usually, grow anti-parallel to the main heat flux direction (perpendicular to layer-layer interface). As mentioned before, the scale of microstructure is variable, and the dendrites size is coarser in such a zone and finer in some others (compare circles A, B in Figure 8c and circle E in Figure 8b). The sizes and type of microstructure can be attributed to the different solidification condition induced by the manual process of deposition. Anyway, the scale of microstructure is in general quite fine due to the high cooling rate of the melt induced by the ESD process.

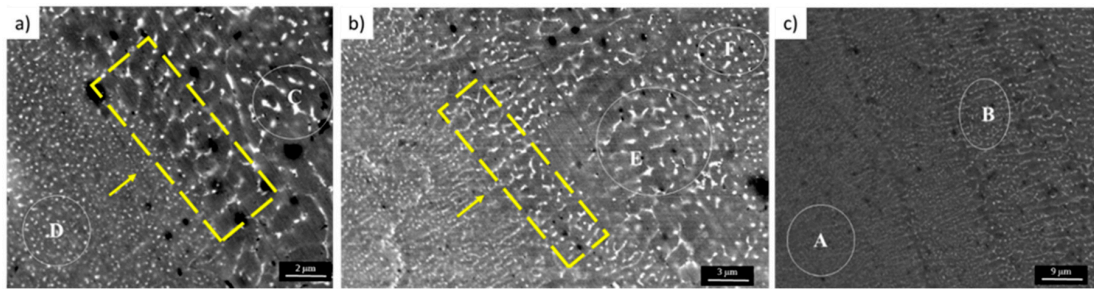


Figure 8. High magnification SEM images of the deposit cross-section showing some different areas inside the deposit. Yellow arrows indicate the microstructure in the layer-layer interfaces. (a) circles C and D highlighted the different microstructures in the different layers; (b) circle E shows dendrites with mixed morphology while the circle F shows uniform distribution of fine second phase particles inside the same layer; (c) circles A and B highlight the same cellular dendritic microstructure in different layers.

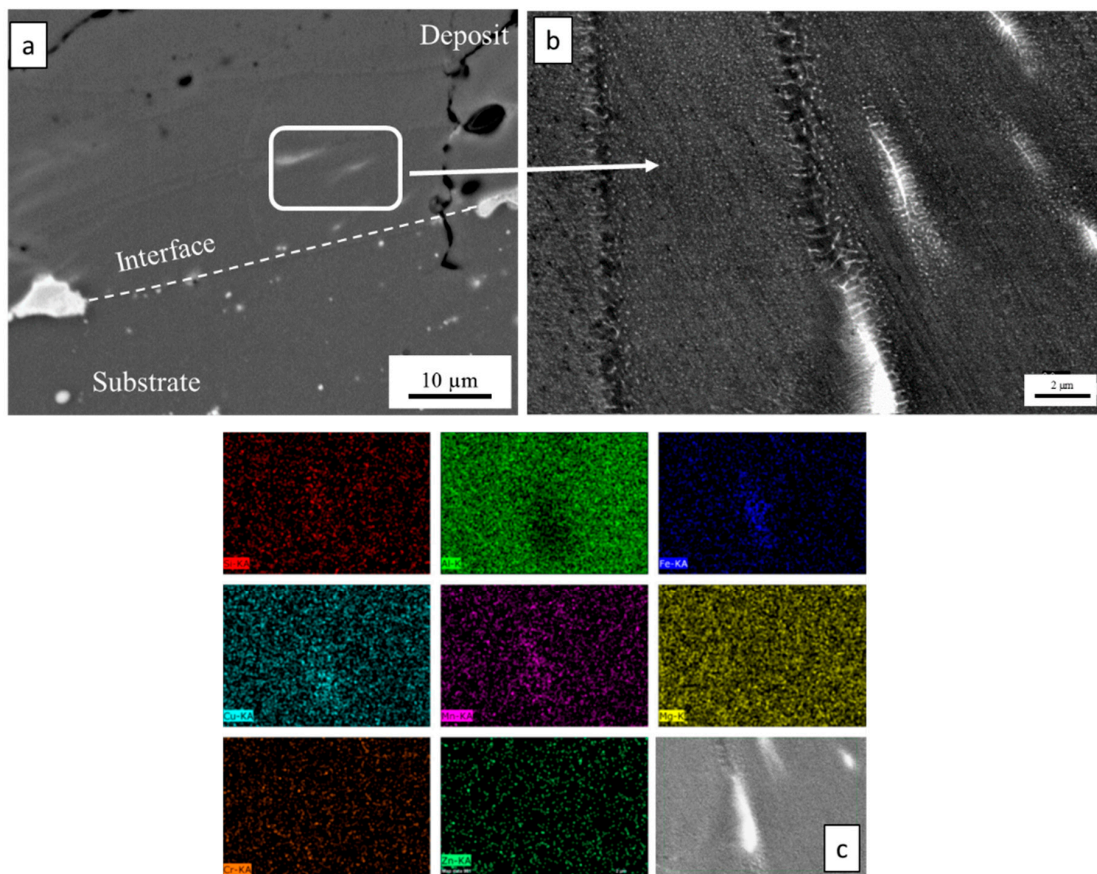


Figure 9. (a) SEM micrograph showing the interface layer between deposit and substrate alloy (b) SEM micrograph (backscattering mode) showing the microstructure of deposit/substrate interface and (c) energy dispersive spectrometry (EDS) map to interface layer.

Figure 9 shows the microstructure near the interfacial region in electrospray deposit. There is a thick interfacial region of about 20 μm between the substrate and the deposit that can be observed (Figure 9a,b). Backscattered electron images reveal that this interfacial region is characterized by large constituent intermetallic particles that are distorted and partially melted surrounded by a high segregation (Figure 9a,b). By EDS analysis (Figure 9c) it was found that those deformed particles are the $(\text{Mn,Fe})_3\text{SiAl}_{12}$ phases coming from the substrate material because of melting and mechanical

mixing of both electrode and base material [25,36]. The base material next to the interface does not present any chemical and microstructural modification or HAZ.

3.4. Mechanical Characterization

The effect of mixed refined microstructure on the hardness values in the deposit cross-section was evaluated by indentations performed both within some layers and at the interfaces between the layers (Figure 10a–e). The indentations on the layer-layer interfaces, as well as on the inner of different layers exhibited different values of micro-hardness as a function of the solidification microstructure. The layer interfaces in Figure 10a,b exhibit values of micro-hardness respectively of 156.4 HV and 132.5 HV. Figure 10c–e shows the value of micro-hardness as equal to 145, 140, 132 HV, respectively. In some cases, the micro-hardness values can also be influenced by micro defects present within the deposit. So, the hardness within the deposit is not constant but strongly variable. Nevertheless, the average hardness values evaluate along lines of indentation parallel to the substrate/deposit interface do not significantly change both with the spark pulse-energy (E_s) and/or with frequency at fixed E_s (Figure 11a–c). Three different average micro-hardness values can be read for each distance as a function of the increasing frequency, except for the deposit fabricated at the lowest E_s and frequency (Figure 11a), where just one line of indentation has been produced due to the reduced thickness of the deposit. Our result, therefore, indicated that the three set values of E_s and frequency do not significantly affect the mechanical behavior of the deposits. Figure 12 shows the average deposit hardness as a function of E_s for F1, F2 and F3. In close accordance with the above results (Figure 11), the average deposits of micro-hardness does not significantly change, indicating that all the ESD parameters sets produce similar microstructures. The average micro-hardness values of the analyzed deposits are in fact distributed in a small range (100–120 HV). Of course, the average hardness values are characterized by high standard deviations due to the great variability of the microstructure. Moreover, the micro-hardness of the substrate close to interface do not exhibit any change, which confirms the absence of a heat affected zone (HAZ).

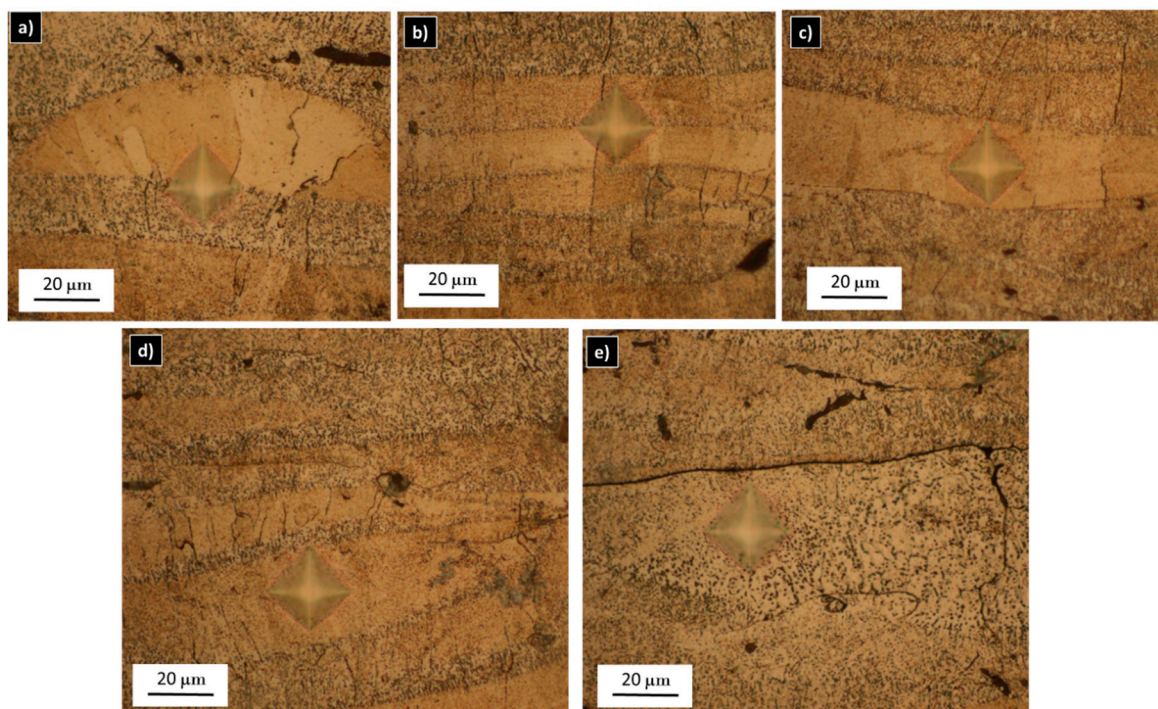


Figure 10. Micro-hardness measurement at a layer-layer interface (a,b); inside some layers with different microstructure (c–e).

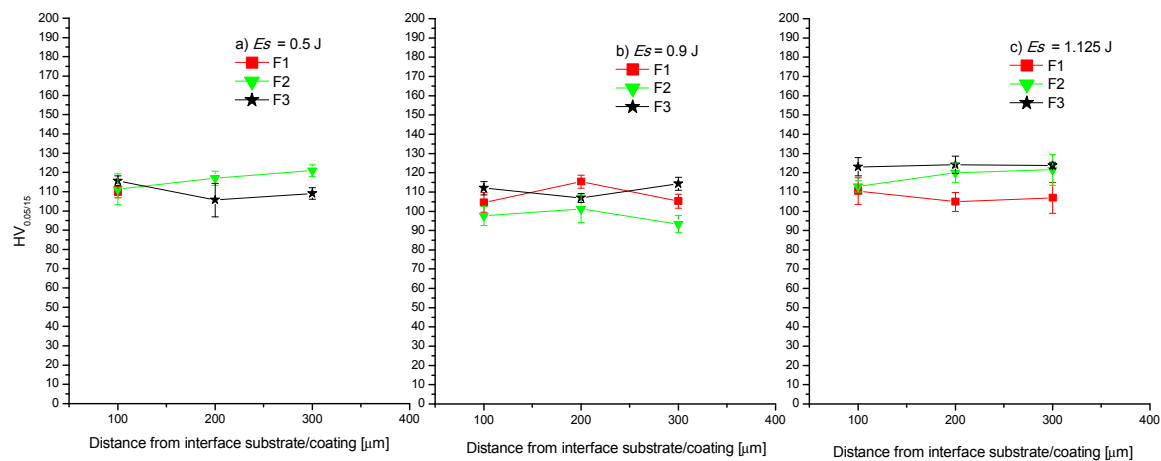


Figure 11. Micro-hardness as a function of the distance from substrate/deposit interface for the different parameters adopted: (a) V1, C2, 10 L/min ($Es = 0.5$ J); (b) V2, C1, 10 L/min ($Es = 0.9$ J) and (c) V2, C2, 10 L/min ($Es = 1.125$ J).

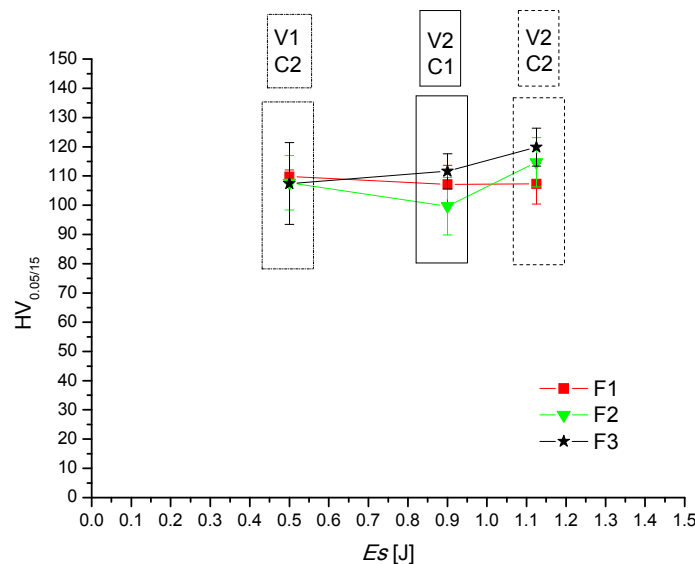


Figure 12. Effect of spark pulse-energy (Es) on micro-hardness for three levels of frequency ($F1 < F2 < F3$).

3.5. Analysis of Defects

Figure 13 presents the percentage (%) of defectiveness in the deposits cross-section as a function of spark pulse-energy (Es) for three values of frequency. The defectiveness levels induced by depositions are considered acceptable, however at lower energy level all the deposits display a greater percentage of defectiveness. The results indicate that the increasing Es (increasing the voltage and decreasing/keeping constant the capacitance) decreases the percentage defectiveness for all three frequencies sets. It is believed that the percentage defectiveness decreases, since a higher Es will produce a higher volume of the molten splat and a higher thickness splat [2,37]. In other words, by increasing the Es the splat becomes larger [38] and the space between the individual splat reduces, leading to lower level of voids. Moreover, with each successive pass, a higher energy allows the re-melting of a greater amount of the deposited material, leading to elimination of the surface roughness (micro-voids) and undulation (peak and valley) previously created [23].

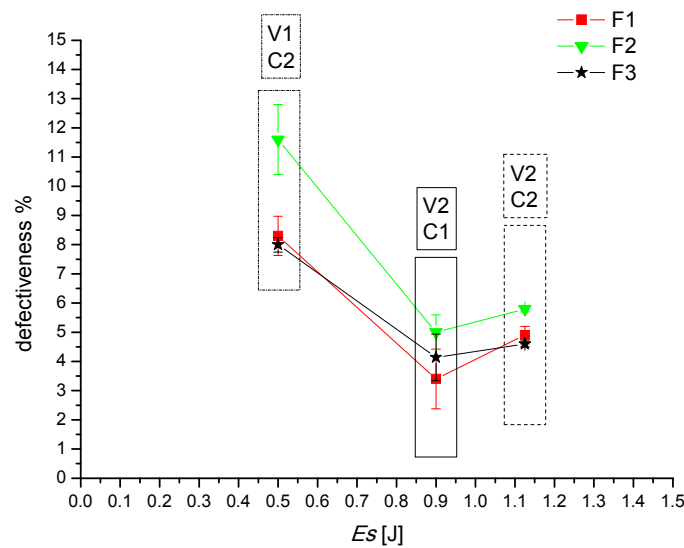


Figure 13. Percentage defectiveness in deposits cross-section as a function of spark pulse-energy (E_s) for three values of frequency ($F1 < F2 < F3$).

Particularly, the voltage value plays a significant role on the percentage defectiveness of the deposit when compared to the other process parameters set. In fact, if the voltage value is increased from V1 to V2 (compare 0.5 J vs. 1.125 J in Figure 13), the level of defectiveness is reduced; while, if the voltage is kept constant (0.9 J vs. 1.125 J in Figure 13), the level of defectiveness does not significantly change. The analysis of the distribution of the defect area observed in the deposits produced at 0.5, 0.9 and 1.125 J is shown in Figure 14. The deposits (Figure 14) are characterized by high percentage of defects having small area. Furthermore, the defects both of small and large areas are reduced when the energy (E_s) increase due to the voltage increment (Figure 14a,b and Figure 14a,c). The defects areas distributions do not change significantly with capacitance (Figure 14b,c).

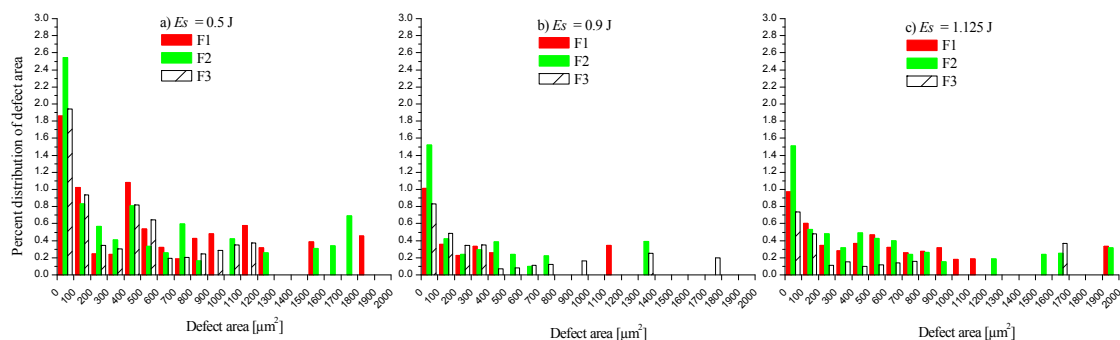


Figure 14. Analysis of the percent distribution of the defect area observed in the deposit at (a) 0.5 J (V1, C2); (b) 0.9 J (V2, C1) and (c) 1.125 J (V2, C2) for different values of frequency $F1 < F2 < F3$.

3.6. Effect of the Parameters Electric on Substrate/Deposit Interface Behavior

It is known that the AA2024 alloy is susceptible to solidification cracks or liquation cracks being characterized by a large solidification range, high thermal expansion, large solidification shrinkage, and a large quantity of alloying addition [9,35]. Solidification cracking occurs during the solidification of melt. It occurs along grain boundaries, and it is due to the shrinkage stress from both molten metal solidification and non-uniform thermal contraction [34,35]. Liquation cracking occurs at a temperature lower than solidus temperature during non-equilibrium heating of the alloy, for example in the HAZ of weld, where the peak temperature of the welding cycle is just below the solidus temperature.

Liquation cracking is due to the combination of constitutional liquation phenomenon [35], (localized grain boundaries melting at temperature significantly below the solidus T of the alloy) and tensile stresses that act on constitutionally liquated areas to produce cracks called liquation cracks. In fact, with the grain boundary liquated, the alloy has little strength to resist tensile stresses. All the ESD parameters set lead to cracks extending into the substrate along the grain boundaries (Figure 15a). Higher magnification SEM images suggest the delineation of the crack paths by re-solidified products, typical of liquation cracking (Figure 15b). During the ESD process, the temperature of the area close to the substrate/deposit interface can promote the melting of some areas (usually, located at intermetallic particle surface and/or at the grain boundaries) where a higher solute concentration develops and locally alters the liquidus (solidus) T of the alloy. Simultaneously, the rapid cooling from the ESD process induces a great thermal strain that opens the liquated zones. Therefore, due to ESD process, those cracks are inevitable on the heat sensitive AA2024 substrate [9,12,39,40]. Once initiated, the cracks propagate along the substrate grain boundary and may also easily propagate in the deposited layers giving rise in a continuous network (Figure 15a). The liquation cracks dramatically reduce the mechanical properties of the substrate, and moreover, limit the feasibility of producing ESD deposits/repair in the 2024 alloy. So, the cracks number, length, and length distributions as a function of ESD process parameters have been investigated in the following.

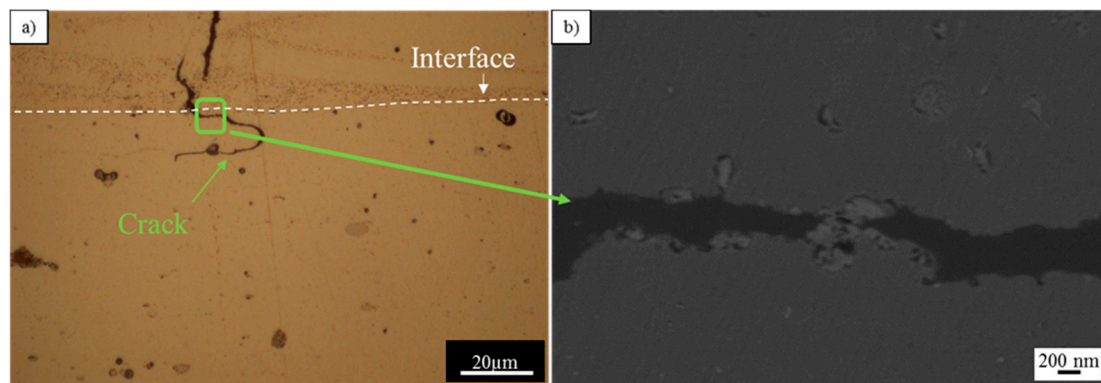


Figure 15. (a) OM micrograph of the deposit/substrate interface showing the crack that propagate in substrate along boundary grain; (b) higher magnification SEM image of liquation cracking.

Figure 16 shows the average cracks length that propagates within the substrate from the substrate/deposit interface as a function of spark pulse-energy (E_s). The analysis of the average cracks length in function of the E_s (Figure 16), shows that the average cracks length increase with E_s . In fact, as E_s increases, a higher heat input is supplied to the substrate favoring both hot cracking and grain boundary liquation of 2024 alloy [6]. Thus, this trend is opposite to that of the defects within the deposits. Specifically, the increase of average crack length is more sensitive to voltage increase in respect to capacity increase. After all, both voltage and capacity increases lead to higher heat input, but the role of voltage on E_s is more significant ($E_s = 1/2CV^2$). Furthermore, it was observed that, for the same E_s the average cracks length increased with the frequency increase.

Figure 17 shows, for all three pulse energy conditions, the cracks length distributions that extend into the base material at increasing frequencies. Specifically, each graph shows the cracks number having a length comprised in classes of fixed amplitude. The analysis of the histograms shows that both the number of cracks and the length variation range tend to rise with the energy discharge. In addition, with increasing frequency, the peak of the distributions tends to shift towards higher lengths (Figure 17b,c). With reference to the results presented through Figures 13, 14, 16 and 17, it appears that the combination of 0.9 J pulse energy and F2 frequency allows to get sufficiently thick deposit and low defectiveness, both inside the deposit and at the interface.

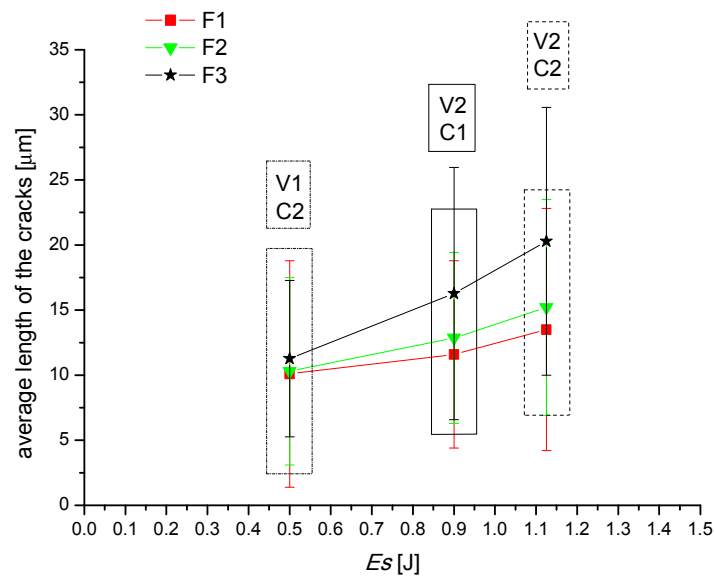


Figure 16. Effect of spark pulse-energy E_s on average cracks length that propagate in the substrate from the deposit/substrate interface for three different values of frequency ($F1 < F2 < F3$).

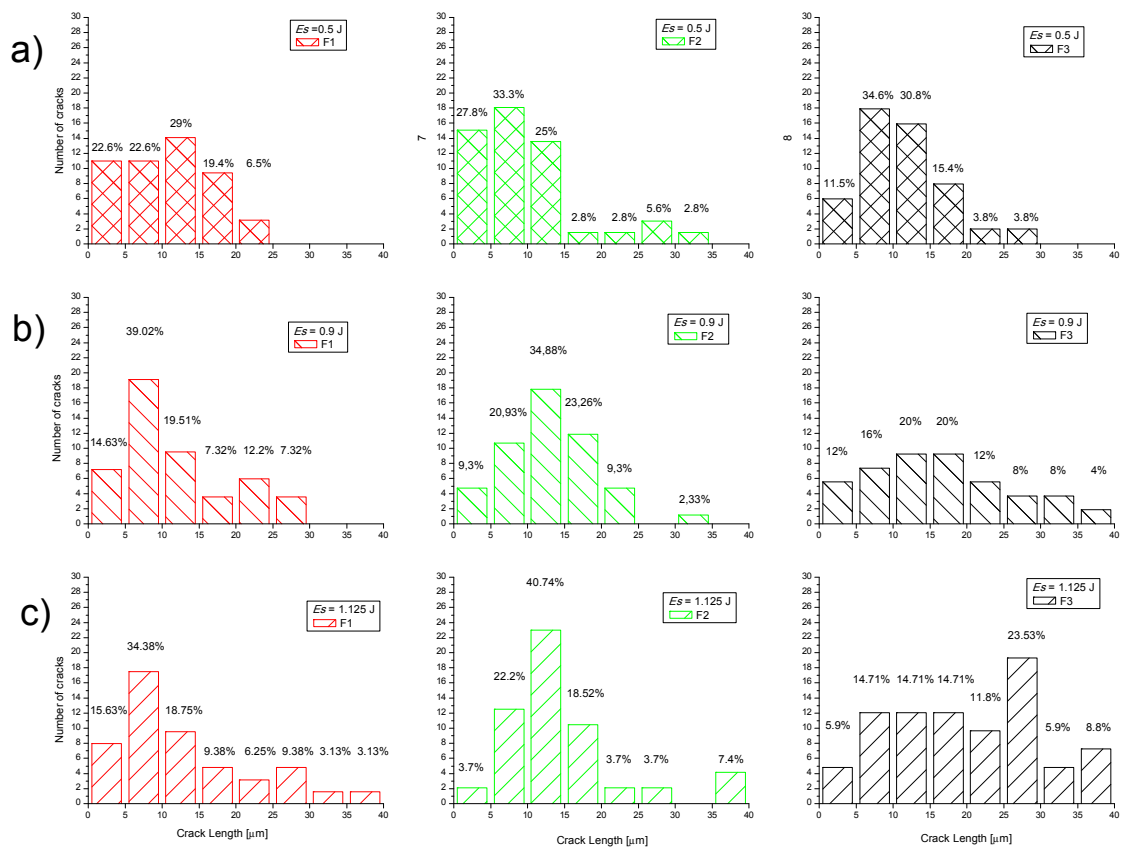


Figure 17. Number of cracks vs. cracks length of multiple-layer deposition produced using: (a) 0.5 J (V1, C2, 10 L/min), (b) 0.9 J (V2, C1, 10 L/min) and (c) 1.125 J (V2, C1, 10 L/min) as a function of the frequency ($F1 < F2 < F3$).

4. Conclusions

In the present study, AA2024 was deposited on homologous substrate by the electro-spark process. The deposits exhibit the following characteristics.

- (1) They have layer-by-layer microstructure, and all layers are characterized by a fine and mixed microstructure both cellular and equiaxed. The cell size is not uniform along the deposit.
- (2) The grains are columnar and parallel to the growth direction of the deposit. Their size is not uniform and they spread through more than one layer whose microstructure is mixed.
- (3) The average hardness values do not change significantly with process parameters. The great standard deviation in average hardness is due to the strong variations microstructural within the thickness.
- (4) The defects have small dimensions whose size reduces with the increasing E_s at a fixed frequency. When increasing the heat input, the defectiveness is reduced due to higher volume of re-melted substrate, the higher volume of molten splat and the lower space between the splats.
- (5) The substrate/deposit interface is characterized by the presence of cracks which extend into the substrate preferentially along the grain boundaries. The average length of cracks increases with frequency and E_s .
- (6) Within the experimental plan developed in this study, the best energy value (E_s) to deposit 2024 alloy on homologue substrate reducing both the inner porosity and the length of the interface cracks, is 0.9 J.

Future studies will focus on the reduction of the defects. For example, the use of automatized depositions could solve the limits due to the manual process and/or a slight heating of the substrate during the depositions could reduce the thermal stresses crack without affecting the deposit/substrate microstructure.

Author Contributions: Paola Leo and Gilda Renna designed research and experiments, handled the microstructure and data analysis; Gilda Renna performed the fabrication of the coatings. Giuseppe Casalino revised the language and commented on the experimental results.

Conflicts of Interest: The authors declare no conflict of interest.

References

1. Frangini, S.; Masci, A. A study on the effect of a dynamic contact force control for improving electrospark coating properties. *Surf. Coat. Technol.* **2010**, *204*, 2613–2623. [[CrossRef](#)]
2. Hasanabadi, F.M.; Ghaini, M.F.; Ebrahimnia, M.; Shahverdi, H.R. Production of amorphous and nanocrystalline iron based coatings by electro-spark deposition process. *Surf. Coat. Technol.* **2015**, *270*, 95–101. [[CrossRef](#)]
3. Campanelli, S.L.; Angelastro, A.; Signorile, C.G.; Casalino, G. Investigation on direct laser powder deposition of 18 Ni (300) marage steel using mathematical model and experimental characterization. *J. Adv. Manuf. Technol.* **2017**, *89*, 885–895. [[CrossRef](#)]
4. Angelastro, A.; Campanelli, S.L.; Casalino, G. Statistical analysis and optimization of direct metal laser deposition of 227-F Colmonoy nickel alloy. *Opt. Laser Technol.* **2017**, *94*, 138–145. [[CrossRef](#)]
5. Verbitchi, V.; Ciuca, C.; Cojocaru, R. Electro-Spark Coating with Special Materials. *Nonconv. Technol. Rev.* **2011**, *1*, 57–62.
6. Davis, J.R. *ASM Specialty Handbook: Aluminum and Aluminum Alloy*; ASM International: Almere, The Netherlands, 1993.
7. Onjukka, R. Welding vs. Riveting—Which Has the Fatigue Life for Airplanes. *Weld. J.* **1996**, *75*, 29–33.
8. Kou, S. *Welding Metallurgy and Weldability of High Strength Aluminum Alloys*; Welding Research Council Bulletin: Madison, WI, USA, 1986.
9. Ghaini, M.F.; Sheikhi, M.; Torkamany, M.J.; Sabbaghzadeh, J. The relation between liquation and solidification cracks in pulsed laser welding of 2024 aluminium alloy. *Mater. Sci. Eng. A* **2009**, *519*, 167–171. [[CrossRef](#)]
10. Norman, A.F.; Drazhner, V.; Prangnell, P.B. Effect of welding parameters on the solidification microstructure of autogenous TIG welds in an Al-Cu-Mg-Mn alloy. *Mater. Sci. Eng. A* **1999**, *259*, 53–64. [[CrossRef](#)]
11. Oates, W.R. (Ed.) *Materials and Applications*, 8th ed.; AWS: Miami, FL, USA, 1972; pp. 1–28.
12. Zhao, H.; White, D.R.; DebRoy, T. Current issues and problems in laser welding of automotive aluminium alloys. *Int. Mater. Rev.* **1999**, *44*, 238–266. [[CrossRef](#)]

13. Cao, X.; Wallace, W.; Immarigeon, J.P.; Poon, C. Research and Progress in Laser Welding of Wrought Aluminum Alloys. II. Metallurgical Microstructures, Defects, and Mechanical Properties. *Mater. Manuf. Process.* **2003**, *18*, 23–49. [[CrossRef](#)]
14. Brochu, M.; Heard, D.W.; Milligan, J.; Cadney, S. Bulk nanostructure and amorphous metallic components using the electrospark welding process. *Assem. Autom.* **2010**, *30*, 248–256. [[CrossRef](#)]
15. Champagne, V.; Pepi, M.; Edwards, B. *Electrospark Deposition for the Repair of Army Main Battle Tank Components*; Army Research Laboratory: Adelphi, MD, USA, 2006.
16. Johnson, R.N. Robust coatings for corrosion and wear: The electrospark deposition process. In Proceedings of the Tri-service conf. on corrosion, Myrtle Beach, SC, USA, 15–19 September 1999; pp. 341–410.
17. Cadney, S. Welding and Weld Repair of Nanostructured and Amorphous Materials. Master's Thesis, McGill University, Montreal, QC, Canada, 2007.
18. Brochu, M.; Portillo, J.G.; Milligan, J.; Head, D.W. Development of Metastable Solidification Structures Using the Electrospark Deposition Process. *Open Surf. Sci. J.* **2011**, *3*, 105–114. [[CrossRef](#)]
19. Perju, M.C.; Vizureanu, P.; Nejneru, C. The study of energy transfer on thin layers achieved by electro-spark deposition with tic electrode. In Proceedings of the International Conference of Scientific Paper Afases, Brasov, Romania, 22–24 May 2014.
20. Thamer, A.D.; Hafiz, M.H.; Mahdi, B.S. Mechanism of Building-Up Deposited Layer during Electro-Spark Deposition. *J. Surf. Eng. Mater. Adv. Technol.* **2012**, *2*, 258–263. [[CrossRef](#)]
21. Liu, D.Y.; Gao, W.; Li, Z.W.; Zhang, H.F.; Hu, Z.Q. Electro-spark Deposition of Fe-based Amorphous Alloy Coatings. *Mater. Lett.* **2007**, *61*, 165–167. [[CrossRef](#)]
22. Xie, Y.J.; Wang, M.C.; Huang, D.W. Comparative study of microstructural characteristics of electrospark and Nd:YAG laser epitaxially growing coatings. *Appl. Surf. Sci.* **2007**, *253*, 6149–6156. [[CrossRef](#)]
23. Xie, Y.J.; Wang, M.C. Epitaxial MCrAlY coating on a Ni-base superalloy produced by electrospark deposition. *Surf. Coat. Technol.* **2006**, *201*, 3564–3570. [[CrossRef](#)]
24. Xie, Y.J.; Wang, M.C. Microstructural morphology of electrospark deposition layer of a high gamma prime superalloy. *Surf. Coat. Technol.* **2006**, *201*, 691–698. [[CrossRef](#)]
25. Chen, C.J.; Wang, M.C.; Wang, D.S.; Liu, Y.M. Study on corrosion characteristic of high-energy micro-arc alloying of Al-Y electrode on AZ31 magnesium alloy. *Trans. Mater. Heat Treat.* **2007**, *28*, 106–110.
26. Heard, D.W.; Brochu, M. Development of a nanostructure microstructure in the Al-Ni system using the electrospark deposition process. *J. Mater. Process. Technol.* **2010**, *210*, 892–898. [[CrossRef](#)]
27. Cadney, S.; Brochu, M. Formation of amorphous $Zr_{41.2}Ti_{13.8}Ni_{10}Cu_{12.5}Be_{22.5}$ coatings via the ElectroSpark Deposition process. *Intermetallics* **2008**, *16*, 518–523. [[CrossRef](#)]
28. Xie, Y.J.; Wang, M.C. Isothermal oxidation behavior of electrospark deposited MCrAlX-type coatings on a Ni-based superalloy. *J. Alloy Compd.* **2009**, *480*, 454–461. [[CrossRef](#)]
29. Xie, Y.J.; Wang, M.C. A feasibility study of preparing MCrAlX/BN composite coatings by electrospark deposition process. *J. Alloy Compd.* **2009**, *484*, 21–24. [[CrossRef](#)]
30. Mondolfo, L.F. *Aluminium Alloys: Structure and Properties*; Butter-Worth: London, UK, 1976.
31. Chen, Z.; Zhou, Y. Surface modification of resistance welding electrode by electro-spark deposited composite coatings: Part I. Coating characterization. *Surf. Coat. Technol.* **2006**, *201*, 1503–1510. [[CrossRef](#)]
32. Wang, J.S.; Meng, H.M.; Yu, H.Y.; Fan, Z.S.; Sun, D.B. Characterization and wear behavior of WC-0.8Co coating on cast steel rolls by electro-spark deposition. *Int. J. Miner. Metall. Mater.* **2009**, *16*, 707.
33. Kurz, W.; Fisher, D.J. *Fundamentals of Solidification*, 4th ed.; CRC Press: Boca Raton, FL, USA, 1998.
34. Porter, D.A.; Easterling, K.E. *Phase Transformations in Metals and Alloys*; CRC Press: Boca Raton, FL, USA, 1992.
35. Messler, R.W., Jr. *Principles of Welding*; John Wiley & Sons: Hoboken, NJ, USA, 1999.
36. Ebrahimnia, M.; Ghaini, M.F.; Xie, Y.J.; Shahverdi, H. Microstructural characteristics of the built-up layer of a precipitation hardened nickel based superalloy by electrospark deposition. *Surf. Coat. Technol.* **2014**, *258*, 515–523. [[CrossRef](#)]
37. Tang, S.K. The Process Fundamentals and Parameters of Electro-Spark Deposition. Master's Thesis, University of Waterloo, Waterloo, ON, Canada, 2009.
38. Tušek, J.; Kosec, L.; Lešnjak, A.; Muhič, T. Electrospark Deposition for Die Repair. *Metalurgija* **2012**, *51*, 17–20.

39. Huang, C.; Cao, G.; Kou, S. Liquation cracking in partial penetration aluminium welds: Assessing tendencies to liquate, crack and backfill. *Sci. Technol. Weld. Join.* **2004**, *9*, 149–157. [[CrossRef](#)]
40. Kou, S. *Welding Metallurgy*; John Wiley & Sons: Hoboken, NJ, USA, 2002.



© 2017 by the authors. Licensee MDPI, Basel, Switzerland. This article is an open access article distributed under the terms and conditions of the Creative Commons Attribution (CC BY) license (<http://creativecommons.org/licenses/by/4.0/>).